Phase Transformation-Induced Changes in Microstructure and Residual Stresses in Thermally Sprayed MnCoFeO$_4$ Protective Coatings

Hyoung Chul Back[1] · Jens Gibmeier[1] · Robert Vaßen[2]

Abstract The contribution comprises the investigation of the microstructure and residual stresses in thermally sprayed $Mn_{1.0}Co_{1.9}Fe_{0.1}O_{4.0}$ (MCF) protective coatings for interconnectors of SOFC stacks, deposited on ferritic steel Crofer 22 APU via atmospheric plasma spraying (APS). The coatings are designated to prevent Cr evaporation during high operation temperature of the SOFCs. The local microstructure, pore distributions and pore shapes, phase fractions, micro-hardness, Youngs' modulus and residual stresses through the coating thickness were characterized in as-sprayed state and compared with longtime (10-100 h) heat-treated samples (700 and 850 °C). The results show that the long-term thermal aging treatment causes a successive high sintering of the coatings characterized by a reduction in pore density, by phase transformation from the metastable rock salt structure that gradually transformed to a spinel structure and by a slight relaxation of the process-induced tensile residual stresses in the coating. For SOFC application of the MCF coating, this indicates an improvement in the coatings integrity. During operation, a self-repair proceeds leading to dense and gas-proof coatings, while the mechanical properties are mainly retained.

✉ Jens Gibmeier
jens.gibmeier@kit.edu

[1] Institute for Applied Materials, Karlsruhe Institute of Technology (KIT), Karlsruhe, Germany

[2] Institute of Energy (IEK-1), Forschungszentrum Jülich GmbH, Jülich, Germany

Introduction

Solid oxide fuel cells (SOFC) are attractive candidates for energy conversion systems for an effective way of producing electrical energy directly from chemical energy. Due to the limited output power, single cells can be arranged into stack system and interconnectors are used to link the individual cells. High-chromium-containing ferritic stainless steels are widely used for interconnectors due to their good electrical conductivity, chemical and mechanical stability, suitable thermal expansion behavior and low cost. However, during high operation temperature these materials form chromia-containing oxide scales on the surface and these scales tend to evaporate especially under water vapor environment. Due to chromium migration into the cathode side, the cell performance can suffer from degradation (Ref 1-3). Protective layers can be applied between interconnector and cathode to suppress the evaporation of Cr from chromium-containing oxide scales, hence to enhance the long-term performance of solid oxide fuel cells (SOFCs). $MnCo_{1.9}Fe_{0.1}O_4$ (in the following designated as MCF) spinel is a promising candidate for protected layer due to the following properties: (a) high electrical conductivity, (b) chemical stability under oxidizing environment up to high operation temperature and (c) suitable thermal expansion coefficient for an interconnector. Atmospheric plasma spraying (APS) is a well-established method for the deposition of these protective layers (Ref 4, 5). For the design and the performance of layers processed through plasma spraying, the effect of

porosity and of process-induced residual stresses must be considered. Residual stresses in plasma-sprayed coatings are induced by the large temperature differences between the molten particles and the substrate during the deposition process and post-deposition process during cooling to ambient temperature, which are divided into so-called thermal stresses and quenching stresses.

When the molten particles are deposited on the substrate, they are quenched to the relatively low substrate temperature T_S, while contraction of deposited particles is constrained by the substrate. In general, this effect leads to tensile (residual) stress in the coating, commonly referred as 'quenching stresses' σ_q. The theoretical quenching stress can be estimated by (Ref 6)

$$\sigma_q = \frac{E_c}{(1 - v_c)} \alpha_c (T_m - T_s) \tag{Eq 1}$$

where E_c is Young's modulus of the coating, α_c the coefficient of thermal expansion of the coating and T_m the temperature of the molten particles (melting temperature). Often, tensile (residual) quenching stresses are significantly reduced by stress relaxation processes, due to microcracking that occurs through exceeding of the local strength and through interfacial sliding due to non-perfect bonding between individual splats and the underlying solidified material (Ref 6). This implies that quenching stresses can hardly be predicted properly.

After deposition, the coating and the substrate will cool down to ambient temperature T_0 and the mismatch in the coefficient of thermal expansion (CTE) between coating α_C and substrate α_S generating thermal (residual) stresses σ_{th}. Depending on the mismatch, the CTE tensile as well as compressive residual stresses can be developed. The mean thermal stresses are given by

$$\sigma_{th} = \frac{E_c}{(1 - v_c)} (\alpha_c - \alpha_s)(T_d - T_0) \tag{Eq 2}$$

with α_s the coefficient of thermal expansion of the substrate, T_d the temperature of the substrate during deposition and T_0 the ambient temperature.

Quenching stresses and thermal stresses are the two main contributions to the residual stress in the coatings, which can be estimated by a simple superposition. However, proper knowledge about residual stresses is essential for the application of the SOFCs since during service thermal cycling occurs that can lead to early cracking and delamination of the coating with respect to the residual stresses induced by the coating process or also due to thermal cycling. Hence, analysis of residual stresses is important to assess the fatigue behavior and the long-term stability of the coatings. Regarding MCF coatings, we

successfully established a measuring and evaluation strategy for depth-resolved residual stress analysis using the incremental hole drilling technique. Here, first measurements indicated that only small residual stresses were induced by the APS processing of MCF coatings (Ref 7).

In general, the microstructure of a thermally sprayed coating is prone to the existence of pores, microcracks, imperfect bonding of single splats and of unmolten particles, which affects the mechanical properties. That means that as a consequence, typically the Young's modulus of a thermal-sprayed coating is lower than the bulk material (Ref 6) and also the strength largely depends on the local microstructure as, e.g., the porosity and the pore (size, orientation) distributions. Furthermore, regarding MCF protective coatings in SOFC applications the operation conditions of SOFCs with thermal exposure and thermal cycling can alter the microstructure appearance of the coating, by which the mechanical properties and possibly also the residual stresses induced by the thermal spraying will change during operation.

Vaßen et al. reported that phase transformation within thermal-sprayed MCF coating occurred during the deposition process and during operation and/or post-treatment, i.e., in air-annealed condition (Ref 4). After heat treatment, the properties of MCF coating significantly changed due to phase transformation and densification processes. However, the x-ray diffraction phase analyses carried out were limited to a near surface region of the coating, i.e., the depth dependence of the phase transformation and hence the microstructure evolution was not further studied but might shed light into the transformation path. Furthermore, experimentally determined residual stresses were not present for the integrated assessment of the transformation behavior.

To deepen the knowledge about the microstructure evolution during thermal exposure of MCF coatings in the present paper, the local microstructures in depth distributions and the elastic properties were determined after annealing at different temperatures and times, which were chosen to simulate typical operation conditions. Furthermore, the residual stress analysis approach used in (Ref 7) was adopted, i.e., the residual stress depth distributions were analyzed by means of incremental hole drilling method to determine the changes in residual stress states in the coating through long-term operation of the MCF coatings. Finally, the results of local residual stress analyses are concatenated with depth-resolved analysis of the local microstructure of MCF coatings for the as-sprayed condition as well as for material states after defined thermal aging to simulate the in-service conditions of MCF protective layers applied in SOFCs.

Experimental Procedures

Manufacture and Thermal Treatment

Preparation of Substrate

The commercial ferritic stainless steel Crofer 22 APU (Thyssen-Krupp VDM GmbH, Werdohl, Germany) was used as substrate material (Ref 8). The chemical composition is given in Table 1. The substrates were first cut by using a laser beam to manufacture samples with dimensions of 25 x 25 x 2.5 mm³. Subsequently, the samples were sandblasted with F150 alumina particles with a size distribution between 60 and 100 μm to improve the adhesion between coating and substrate (Ref 9). The average roughness value (R_a) of the substrate after sandblasting was about 4.3 ± 0.6 μm.

Preparation of $Mn_{1.0}Co_{1.9}Fe_{0.1}O_{4.0}$ Coating Materials

As coating material, a manganese-cobalt-iron oxide spinel powder (H.C. Starck, Laufenberg, Germany) was used with a chemical composition of 23.5 wt.% Mn, 47.6 wt.% Co, 2.4 wt.% Fe and 26.5 wt.% O (MCF), with associated stoichiometry $Mn_{1.0}Co_{1.89}Fe_{0.10}O_{3.88}$ (Table 1). The particle size distribution is characterized by $d_{10} = 14$ μm, $d_{50} = 27$ μm and $d_{90} = 50$ μm with a particle analyzer of type Horiba-LA-950 V2 (Retsch Technology GmbH, Haan, Germany) (Ref 10).

Atmospheric Plasma Spraying

The atmospheric plasma spraying (APS) was performed using a TriplexPro210 gun with a 9-mm nozzle at a power of 49 KW within a multi-coat facility (Oerlikon Metco, Wohlen, Switzerland). An approximately 100-μm-thick MCF coating was deposited using a current of 400 A and a flow rate of 50 NLPM (normal liter per minute) argon and 4 NLPM helium. The standoff distance was 150 mm (Ref 10). Before deposition process, the substrate was preheated at a temperature 200 °C.

Thermal Treatment

After coating, the samples were heat-treated under ambient atmosphere for 10 h at 700 °C, 100 h at 700 °C and 100 h at 850 °C. The heat treatment temperature at 700 °C is the standard SOFC operating condition. In order to investigate the influence of heat treatment time, the samples were heated for 10 and 100 h, respectively. Heat treatment at 850 °C simulates the Jülich SOFC stacks for sealing with glass (Ref 10). In Table 2, the coefficients of thermal expansion (CTE) of substrate and coating are listed.

Characterization of Coatings

Characterization of Microstructure and Pores

For metallographic preparations, the sectioned samples were embedded in epoxy resin. Grinding and polishing was performed by using a semiautomatic grinder polisher (EcoMet 250, Buehler, USA) using a continuously decreasing grit size. The finishing was done using a 1 μm diamond suspension.

Finally, for SEM analyses the polished samples were cleaned in ethanol for 1 min each. The samples were sputtered with gold in order to guarantee electrical conductivity for investigation with a scanning electron microscope (SEM; Zeiss 1540XB, Carl Zeiss, Oberkochen, Germany). Subsequently, the cross sections were characterized using SEM and porosity, and pore sizes and pore shapes were determined by image analysis using the image processing software ImageJ (Ref 11).

X-Ray Diffractometer

The phase evolution and composition of MCF coatings were investigated using a x-ray diffractometer (XRD) with V-filtered Cr K_α radiation (wavelength $\lambda = 2.29$ Å). As primary aperture, a pinhole collimator with a nominal diameter of 1 mm was used. On the secondary beam path, a 2-mm slit was used in front of the point detector.

The measurements were performed on the surface of the samples. The scan range for diffraction analysis was from 50° to 140° in 2Θ with a step size of 0.02°. Subsequent to the x-ray diffraction scan, a careful surface layer removal was performed through a manual grinding using a SiC polishing grit paper (P2500) and the corresponding layer removal was measured using a dial indicator gage. This procedure, which is scan on the surface and careful layer removal, was repeated until the interface between MCF and substrate was reached. The approximate layer removal per

Table 1 Chemical composition of substrate and coating (Ref 8, 9)

Material	Chemical composition, wt.%								
	Fe	Cr	Co	Mn	Ti	Al	Si	La	O
Crofer 22 APU	76.5	22.8	…	0.4	0.7	<0.01	0.02	0.09	…
MCF	2.4	…	47.6	23.5	…	…	…	…	26.5

step was about 10 μm. The x-ray diffraction scan data were refined based on a Rietveld refinement using the MAUD software (Ref 12). The overall background was fitted using the fifth degree polynomials. The calculation of the phase transformation within MCF was based on the changes of structure and lattice parameters as described in (Ref 13).

Hardness Test

To determine the through thickness Young's modulus (*E*-modulus) profile of the MCF coatings, micro-hardness measurements were performed using a micro-hardness testing system (Fischerscope H100V, Helmut Fischer GmbH, Germany) (see Fig. 1), equipped with a Vickers diamond tip. The spatial resolution of the micro-hardness measurement is limited by the size of the indentation, and concerning these boundary conditions must be fulfilled regarding the distances to adjacent indentations and to the edge of the layers. In order to overcome this limitation and to reach a better depth resolution, the micro-hardness tests were realized on an oblique section of the samples that were embedded in epoxy resin in diameter 30 mm with an angle of inclination of α (see Fig. 1). The coating thickness and angle of inclination among the different samples are listed in Table 3.

All micro-hardness measurements were performed employing a load of 100 mN with a constant load rate of 5 mN/s^{-1}. The Young's moduli (*E*) were determined from the slope of the unloading curve. To guarantee a sufficient statistics for each line representing a distinct distance to the sample, at least 10 micro-hardness measurements were carried out per depth coordinate. The value of the Poisson's ratio (*v*) for the MCF was about 0.36, which was determined using ultrasonic spectroscopy (Ref 7).

Residual Stress Depth Profile analysis by Means of Incremental Hole Drilling Method

Residual stress analyses were carried out using the incremental hole drilling method, which is standardized in its standard formulation by the ASTM E837-13 (Ref 14, 15).

In this work, a self-constructed drilling device was applied that enables an orbital drilling process, which is superior for this kind of studies over conventional drilling. For these kinds of hard layers, we found out that orbital drilling avoids local delamination or spalling of the coatings in the vicinity of the hole, which can result in non-meaningful strain readings during stepwise drilling the hole. A TiN-coated end mill with a nominal diameter of ϕ 0.8 mm was used for incremental drilling. In order to obtain an accurate stress distribution, the orbital drilling was conducted by carrying out successive drilling a hole with a final nominal diameter of ϕ 1.8 mm in steps of 10 μm in depth until the substrate was reached. The strain relaxations, which result from redistribution of residual stresses due to removal of MCF material, were measured

Table 2 Coefficients of thermal expansion (CTE) of MCF coatings and substrate

Material	CTE, 10^{-6} K^{-1}
Ferritic steel (Crofer 22 APU)	11.9 (Ref 8)
Protective layer (MCF)	13.4 (Ref 4)

Table 3 Details of coating thickness and angle of inclination

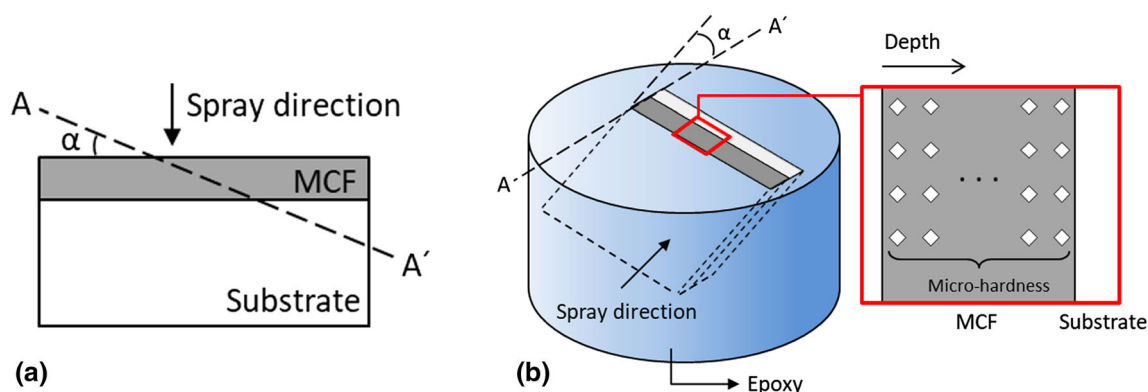| Condition	Coating thickness, μm Cross section	Angle of inclination α, °
As-sprayed	60	10
10 h 700 °C	100	9
100 h 700 °C	70	9
100 h 850 °C	70	8

Fig. 1 Schematic view of the (a) cross section and (b) location used for micro-hardness testing on the oblique section

after each incremental drilling step using strain gage rosettes of type CEA-06-0062-UM-120 (Vishay Measurements Group, Ltd., UK). The residual stress evaluation according to the standard procedures describes, e.g., in the ASTM E837-13, that the incremental or the differential approach in their standard formulation cannot be applied in the present case of an inhomogeneous material. In (Ref 16), a methodology was proposed to determine residual stress depth distributions by means of incremental hole drilling for thick film systems based on case-specific calibration data. In this work, the case-specific calibration data were determined for the MCF coating system by means of finite element (FE) simulations using the software package ABAQUS. The residual stresses were calculated using elastic constants, which were determined by means of instrumented indentation tests. For further details about the simulations, it is referred to (Ref 16).

Results and Discussion

Morphology and Phase Transformation for MCF Coating

In Fig. 2(a)-(d), backscattered electron (BSE) SEM images from cross sections of MCF-coated Crofer 22 APU before and after three different heat treatments are shown. The average porosity of all samples, which were determined by means of image analysis of these BSE images, is given in Fig. 5. The coating thickness varies among the different samples between 60 and 100 μm (see Table 3).

The images indicate that two types of pore shapes can be observed in the MCF coatings: One shows a more globular shape and the other one shows a more lamellar shape. Typically, the globular shape pores are originated from non-proper filling of the volume during spraying in combination with gas entrapment effects while the lamellar-shaped pores are formed as a result of imperfect adhesion of splats or due to local relaxation of mechanical stresses. The size–shape distributions of the determined pores in the MCF coatings are presented in Fig. 4. Here, the shape factor is defined as:

$$\text{shape factor} = \frac{\pi \, (\text{area})}{\text{perimeter}^2} \quad \text{(Eq 3)}$$

In this respect, a shape factor of approximately zero indicates a very flat shape like crack and a value of 1 indicates a circular or globular shape.

A BSE image of a sample in the as-sprayed condition is shown in Fig. 2(a). Analysis of the image indicates that the inhomogeneities are most likely very flat shape pores or microcracks (see Fig. 4a). In Fig. 2(b), the BSE image of a sample is shown that was subjected to a heat treatment for

10 h at 700 °C. The image indicates that almost no microcracks are visible and the MCF coating is obviously densified by the annealing process. In comparison with the as-sprayed condition, the MCF coating is characterized by a two-phase microstructure, i.e., a lighter gray phase and a darker gray phase. Furthermore, pores with a more globular shape and pore sizes smaller than about 2 μm^2 can be observed (see Fig. 4b). Further heat treatment for 100 h at 700 °C also indicates globular pore shapes with particularly small pores at the top surface of the coating (see Fig. 2c and 4c). In addition, thermally grown oxide scale with a darker contrast phase at the interface between the Crofer 22 APU substrate and the MCF coating can be observed for this sample state, both showing a brighter contrast. The average oxide scale thickness is measured to be about 1.6 ± 0.8 μm and was determined by measuring at 10 different positions at the cross section (average values are shown). Figure 2(d) shows the BSE image of the sample heat-treated for 100 h at 850 °C. In comparison with the sample annealed for 100 h at 700 °C, a more homogeneous gray tone exists and indicates that a more homogeneous phase structure is achieved. Furthermore, it appears that the surface region is more densified and that obviously a higher pore density exists in larger depth toward the interface between MCF coating and Crofer 22 APU substrate (Table 4).

Figure 2(e)-(h) presents the x-ray diffractograms of four different depth positions of each sample that was measured after successive polishing from the top surface toward the respective depths. Table 3 summarizes the results of XRD analysis based on a Rietveld refinement. It is assumed that due to the low Fe content the MCF coating system could be represented as a Mn-Co-O system as a good approximation (Ref 17). All diffraction peaks of the sample for the as-sprayed condition were indexed as a cubic salt rock phase (Fig. 2e).

These results of the XRD phase analyses indicate that the cubic spinel $Mn_{1.0}Co_{1.9}Fe_{0.10}O_4$ phase is transformed into the metastable salt rock (Mn,Co,Fe)O phase during atmospheric plasma spraying. Here, no obvious phase gradient in depth is observed (Fig. 3a). The average porosity (average porosities are given in Table 6) of the as-sprayed condition is about 11.3%. Regarding the XRD results, it seems that due to rapid cooling from the molten state to the substrate temperature no cubic spinel phase recovered. In contrast, the diffractograms after 10 h at 700 °C indicate the coexistence of three phases, i.e., the salt rock (Mn,Co,Fe)O phase, high-cobalt-containing cubic spinel $Mn_xCo_{3-x}Fe_{0.10}O_4$ phase ($x \leq 1$) and the low-cobalt-containing cubic spinel $Mn_xCo_{3-x}Fe_{0.10}O_4$ phase ($x \geq 1$) (Fig. 2f). The cobalt content was determined by the lattice parameter according to the literature (Ref 13).
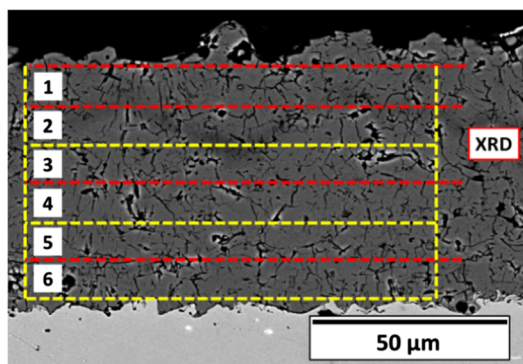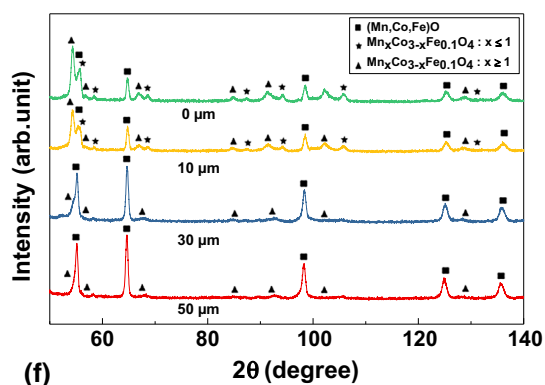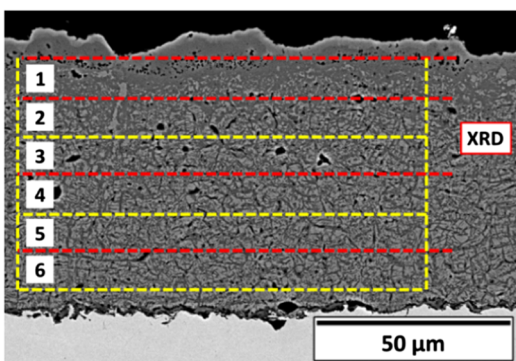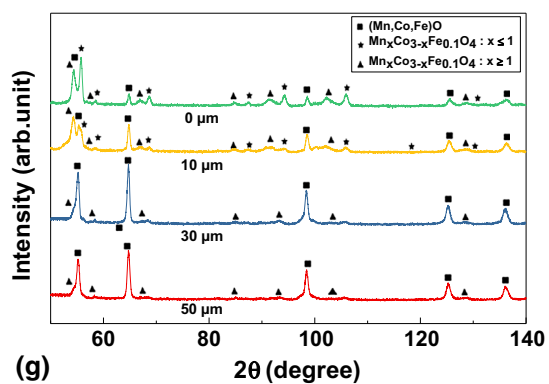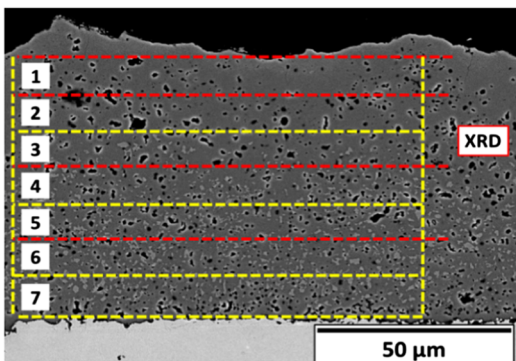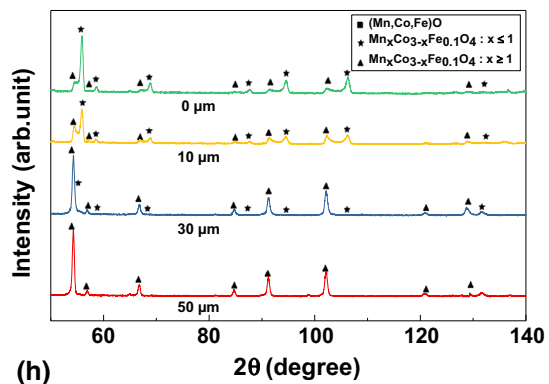
(a) as sprayed
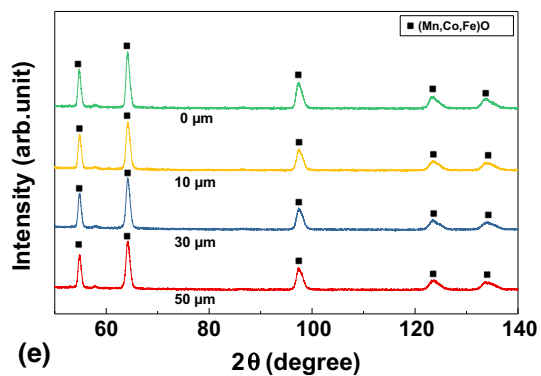
(e)
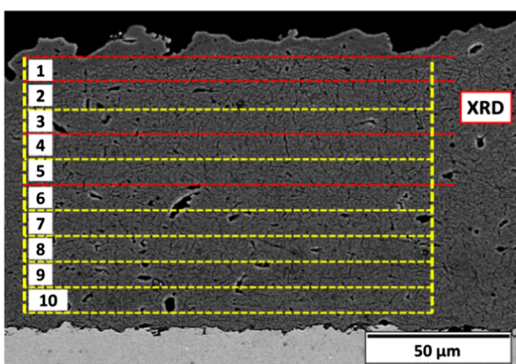
(b) 10h 700 °C

(f)

(c) 100h 700 °C

(g)

(d) 100h 850 °C

(h)

◄ **Fig. 2** BSE images of cross sections of MCF coatings on Crofer 22 APU interconnectors (a)-(d) and x-ray diffractograms determined for different distances to the surface (e)-(h). For each samples, the depths are marked by red dashed lines (BSE images). The areas used for calculation of the porosities are marked by yellow dashed line and are numbered (Color figure online)

On the top surface, about 80% cubic spinel $Mn_xCo_{3-x}Fe_{0.10}O_4$ phase and about 20% cubic salt rock $(Mn,Co,Fe)O$ phase are calculated by means of the Rietveld refinements (Fig. 3b). With increasing distance from the surface, the volume fraction of the cubic spinel $Mn_xCo_{3-x}Fe_{0.10}O_4$ phase is decreased gradually, hence in a depth of about 50-µm cubic salt rock $(Mn,Co,Fe)O$ phase is the main phase of the MCF coatings (Fig. 3b). Furthermore, no more high-cobalt-containing cubic spinel $Mn_xCo_{3-x}Fe_{0.10}O_4$ phase ($x \geq 1$) can be observed in a depth of about 30 µm. The diffractograms for samples annealed for 100 h at 700 °C are shown in Fig. 2(g), and the corresponding volume fraction of the phases is presented in Fig. 3(c). The results indicate that at the sample surface larger fraction of the high-cobalt-containing cubic spinel $Mn_xCo_{3-x}Fe_{0.10}O_4$ phase ($x \geq 1$) exists in contrast to the low-cobalt-containing cubic spinel phase. Furthermore, it can be seen that the volume fraction of the cubic spinel $Mn_xCo_{3-x}Fe_{0.10}O_4$ phase gradually decreases until the depth of approx. 30 µm, and no further significant phase transformation can be noticed in the distance from the surface of about 50 µm.

Additionally, for annealing for 100 h at 700 °C a porosity of approx. 4% is determined near the surface, while with increasing distance to the surface the porosities reduced to about 1% (see Fig 3c). The average porosity for the MCF states annealed at 700 °C for 10 and 100 h is about 2.1 and 1.9%, respectively (see Table 6).

Finally, the diffractograms of the sample after 100 h at 850 °C heat treatment are shown in Fig. 2(h). The data show that only the cubic spinel $Mn_xCo_{3-x}Fe_{0.10}O_4$ phase exists (see Fig. 3d). Up to the depth of approx. 10 µm, diffraction data indicate the presence of about 70% high-cobalt-containing cubic spinel $Mn_xCo_{3-x}Fe_{0.10}O_4$ (with $x \leq 1$) (see also Table 3).

Analysis of the pore distribution indicates that at the surface of the 100 h at 850 °C thermally aged sample the porosity is about 2%. In larger distance to the surface, the porosity increases and reaches a value of about 7% near the interface between MCF coating and Crofer 22 APU substrate. The average porosity is about 4.1% (see Table 6). The increase in porosity in a later state of annealing was attributed to a Co outward diffusion (Ref 10). In Fig. 4, the pore volume fraction is contoured in regard to pore size (y-axis) and shape factor (x-axis). The data indicate that for the as-sprayed condition an accumulation of larger pores with a more lamellar shape (shape factor <0.2) is formed in coexistence with an accumulation of smaller pores (<1 µm) that exhibit a shape factor between about 0.35 and 0.4. After 10-h thermal aging at 700 °C (Fig. 2b), the pore distribution changes. The pore density decreases significantly and the pore distribution is shifted to the right, i.e., toward larger shape factors indicating more globular pore shapes. This behavior is intensified by continuation of the thermal aging at 700 °C to 100 h. The same tendency can be deduced for the MCF coating thermally aged at 850 °C for 100 h. Here, an accumulation of small pores with a more globular form (shape factor between 0.85 and 1) can be observed.

In brief, it has been found regarding the results of x-ray diffraction and porosities analysis that phase transformation and the evolution of the porosity show a mutual relationship and depend on the applied heat treatment conditions. As a result of the thermal aging, a significant reduction in pore density occurs indicating a high sintering effect. Furthermore the data show that the microstructure development through the annealing procedure cause in-depth gradients of phase fraction and porosity distribution. It seems obvious that phase transformation and densification of the coating layer are thermally activated due to diffusion processes.

For the temporal microstructure evolution, the following explanation attempt is proposed: The rock salt structure within the MCF coating that exists through the coating thickness for the as-sprayed condition is not stable below 1050 °C, and during the thermal treatments applied here, the MCF coating tries to reach its stable configuration, i.e., the spinel structure. The proceeding phase transformation can be described by (Ref 17):

$$3(Mn, Co, Fe)O + \frac{1}{2}O_2 \rightarrow (Mn, Co, Fe)_3O_4 \qquad \text{(Eq 4)}$$
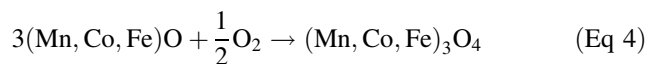
This reaction is dependent on partial oxygen pressure and can cause oxygen uptake that leads to a volume expansion. This chemical reaction occurs preferably at the surface or in the vicinity of pores, which reveal a high oxygen partial pressure. Therefore, in case of low oxygen partial pressure the phase transformation tendency decreases gradually.

Mechanical Properties Evaluation

Regarding the physical and mechanical properties of MCF systems, Table 5 shows a list of coefficients of thermal expansion (CTE) and Youngs' modulus of the different phases of the MCF coatings, i.e., the salt rock structure and the spinel structures, as reported in the literature (Ref 4, 20, 21).

Table 4 Results of Rietveld refinement applied on data of x-ray diffraction analysis carried out on MCF coatings, which are subjected to different heat treatment processes in comparison with the as-sprayed condition

| Condition	Phase	Lattice constant, Å				Volume fraction, vol.%			
		Distance from surface, μm				Distance from surface, μm			
		0	10	30	50	0	10	30	50
As-sprayed	(Mn,Co,Fe)O	4.31	4.30	4.30	4.30	100	100	100	100
10 h 700 °C	(Mn,Co,Fe)O	4.28	4.28	4.28	4.28	20	25	59	81
	$Mn_xCo_{3-x}Fe_{0.10}O_4$ ($x \leq 1$)	8.13	8.13	…	…	23	19	…	…
	$Mn_xCo_{3-x}Fe_{0.10}O_4$ ($x \geq 1$)	8.31	8.32	8.29	8.22	57	56	41	19
100 h 700 °C	(Mn,Co,Fe)O	4.28	4.27	4.28	4.28	10	23	64	66
	$Mn_xCo_{3-x}Fe_{0.10}O_4$ ($x \leq 1$)	8.12	8.12	…	…	36	13	…	…
	$Mn_xCo_{3-x}Fe_{0.10}O_4$ ($x \geq 1$)	8.31	8.34	8.27	8.28	53	64	36	34
100 h 850 °C	$Mn_xCo_{3-x}Fe_{0.10}O_4$ ($x \leq 1$)	8.14	8.16	8.16	…	82	70	3	…
	$Mn_xCo_{3-x}Fe_{0.10}O_4$ ($x \geq 1$)	8.29	8.31	8.33	8.33	18	30	97	100
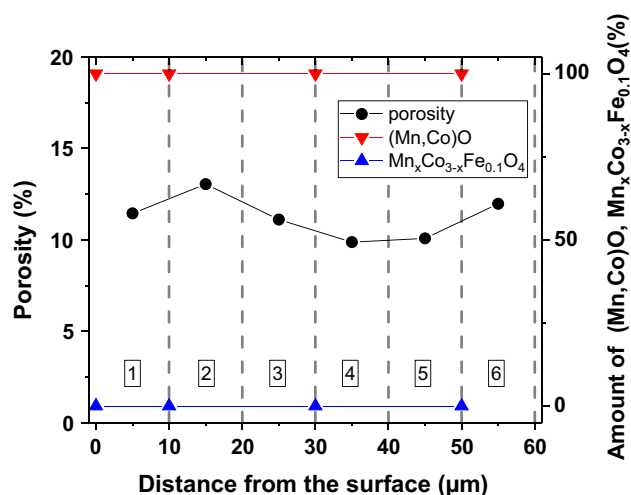
(a) as sprayed
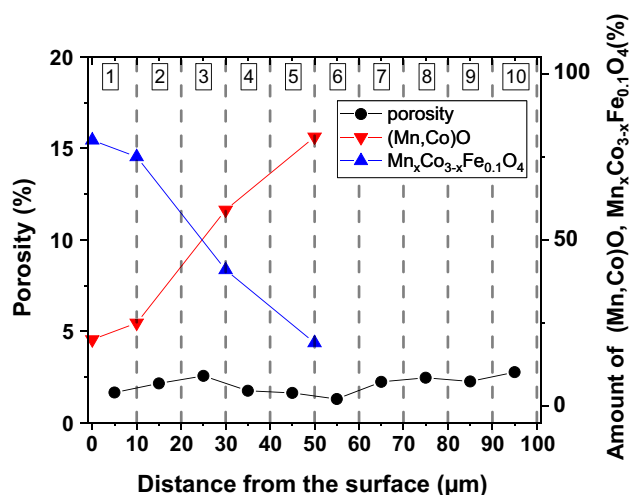
(b) 10h 700 °C
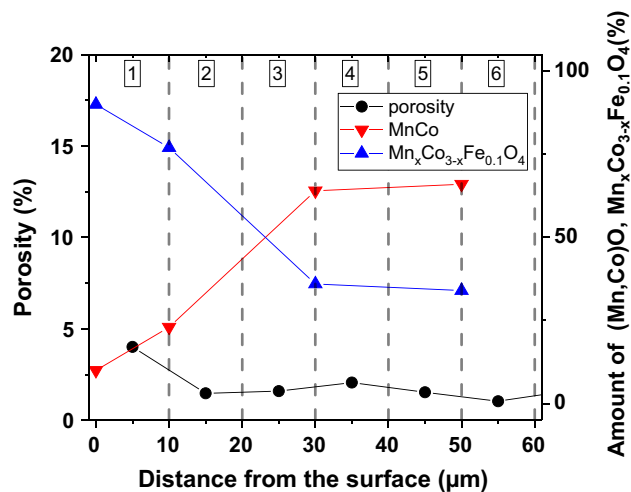
(c) 100h 700 °C
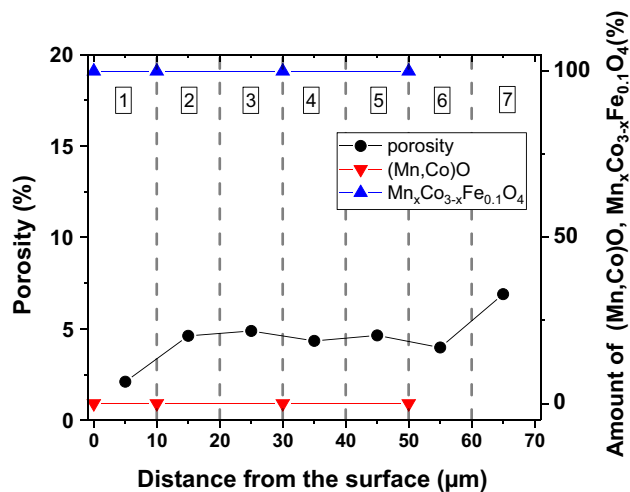
(d) 100h 850 °C

Fig. 3 Porosity depth distribution and depth distribution of the volume fraction of salt rock and spinel structure within the MCF coating for different annealing treatments
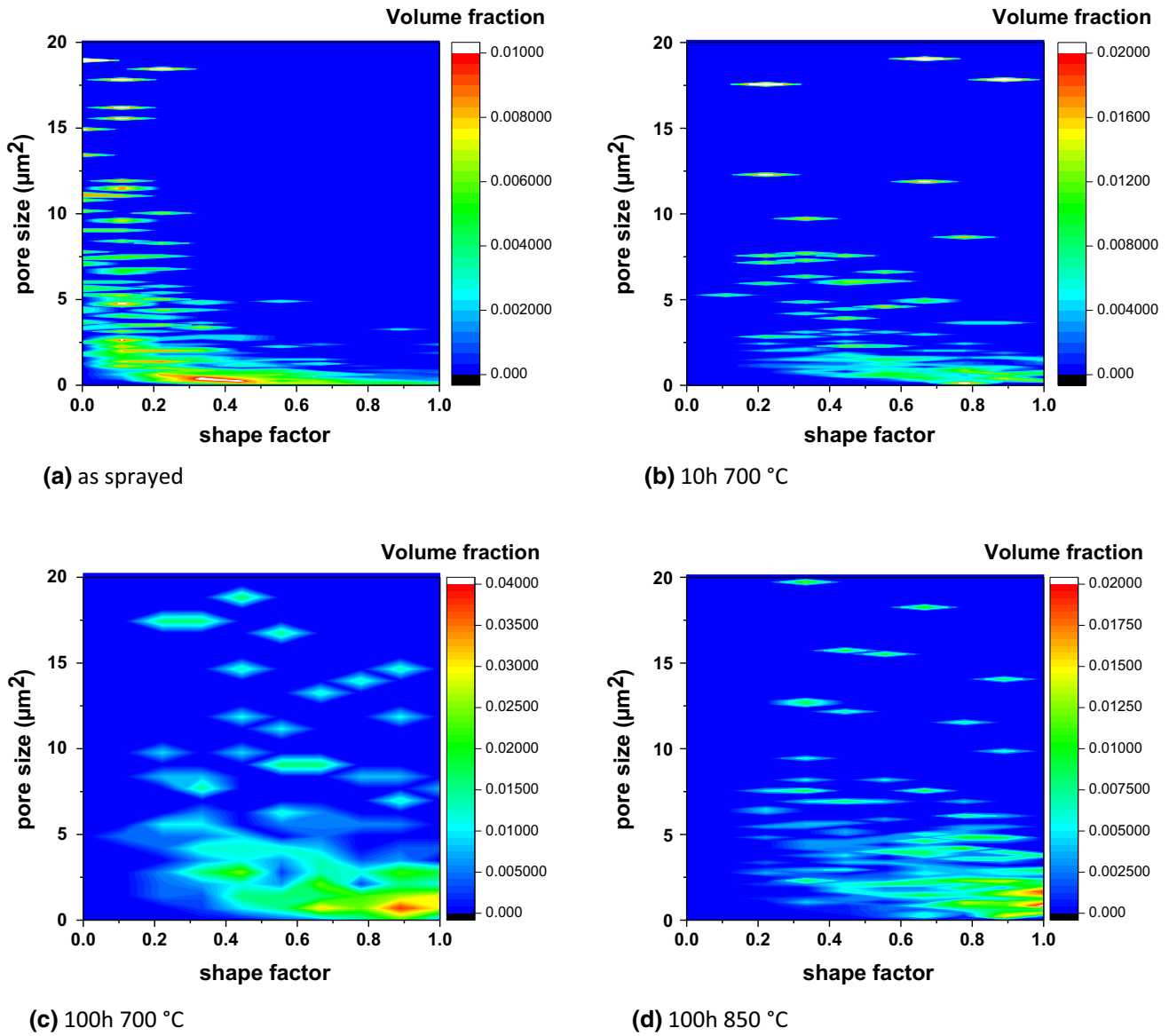
(a) as sprayed

(b) 10h 700 °C

(c) 100h 700 °C

(d) 100h 850 °C

Fig. 4 Distribution statistics of pore size vs. pore shape factor for the annealed MCF coating samples in contrast to the as-sprayed condition

Table 5 E-modulus and coefficient of thermal expansion (CTE) of the salt rock structure (MnO, CoO) and the spinel structure (MnCo$_2$O$_4$) reported in the literature

	E-Modulus, GPa	CTE, 10^{-6} K^{-1}
MnO	222 (Ref 18)	15.0 (Ref 19)
CoO	255 (Ref 18)	15.4 (Ref 20)
MnCo$_2$O$_4$	200 (Ref 4)	13.4 (Ref 4)

As discussed in the previous section, MCF coatings exhibit an inhomogeneous microstructure with pores and show phase transformations, when subjected to defined high-temperature heat treatments, with the result that the microstructure gradually changes with respect to the distance from the surface. In particular, a transition from the salt rock structure to the spinel structure can be observed as a consequence of the heat treatments (Fig. 3). In Table 6, the results of average porosity and phase fraction for the different depths of MCF coatings subjected to different heat treatment processes are summarized.

For the assessment of the mechanical behavior and for the evaluation of residual stresses by means of incremental hole drilling, the effect of the graded microstructure on the depth-dependent materials behavior as, e.g., the effective local stiffness, is of particular interest. The depth distributions of the E-modulus were determined on oblique sections of the coatings by means of instrumented indentation testing and a test load of 100 mN for the as-sprayed

condition in comparison with defined heat-treated states. The results are plotted in Fig. 5 together with the local porosity and volume fractions of the phases. The mean values of the local Young's modulus estimated from instrumented indentation testing are summarized in Table 7.

The data show that due to the relative large porosity of the as-sprayed material rather small value for the local E-modulus was determined ranging around about 110 GPa. Heat treatments for 10 and 100 h at 700 °C cause a significant increase in the Youngs' modulus whereas after heat treatment for 100 h at 850 °C much lower stiffness data were determined, which are only slightly above the

Table 6 Experimentally determined porosity and volume fraction of rock salt and spinel phase through the thicknesses of the coatings for samples subjected to defined heat treatments and for the as-sprayed condition

Condition	Volume fraction, vol.%								Porosity, %
	(Mn,Co,Fe)O				$Mn_xCo_{3-x}Fe_{0.10}O_4$				
Distance from surface, μm	0	10	30	50	0	10	30	50	
As-sprayed	100	100	100	100	0	0	0	0	11.3 ± 1.2
10 h 700 °C	20	25	59	81	80	75	41	19	2.1 ± 0.5
100 h 700 °C	10	23	64	66	90	77	36	34	1.9 ± 0.9
100 h 850 °C	0	0	0	0	100	100	100	100	4.1± 1.5

(a) as sprayed

(b) 10 h 700 °C

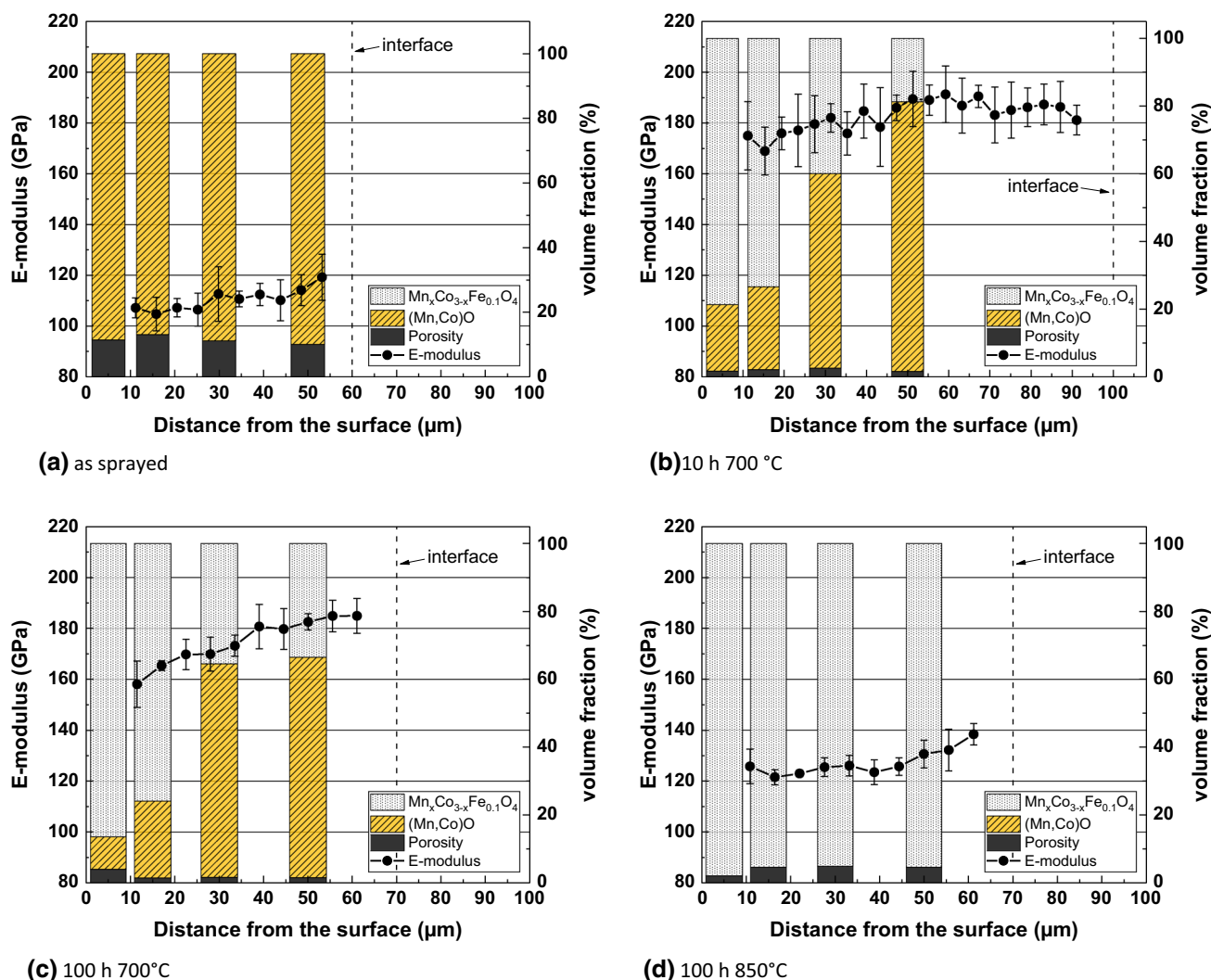**(c)** 100 h 700°C

(d) 100 h 850°C

Fig. 5 Depth distributions of the local Young's modulus in comparison with the depth-dependent courses of the local volume fraction of salt rock and spinel structure as well as the porosity within the MCF coating

Table 7 Experimentally determined Youngs' modulus estimated from instrumented indentation testing of the MCF coating

	Young's modulus, GPa	Poisson's ratio
As-sprayed	110	0.37
10 h 700 °C	182	
100 h 700 °C	174	
100 h 850 °C	127	

values that were recorded for the as-sprayed condition. Hence, the results indicate that the local material stiffness of the MCF coatings is strongly affected by the heat treatment conditions, i.e., by the phase transformations and by the densification (porosity change). In detail, the Young's modulus after heat treatments for 10 h at 700 °C (mean value ≈ 182 GPa) is slightly higher than for 100 h at 700 °C (mean value ≈ 174 GPa), although for both samples almost similar porosities were measured. This and the fact that for the sample heat-treated for 100 h at 700 °C, a steeper gradient of the E-modulus toward lower values at the very surface occur can be explained by the gradual process of phase transformations. In general, the salt rock structure (MnO, CoO) has higher Young's modulus than the spinel structure ($MnCo_2O_4$) (see Table 5). The salt rock (Mn,Co,Fe)O phase is transformed into the spinel structure($MnCo_2O_4$) gradually with increasing distance from the surface. Due to this after heat treatments for 100 h at 700 °C, lower values for the Young's modulus near the surface were determined in contrast to the sample only heat-treated for 10 h at 700 °C. After full-phase transformation from the salt rock (Mn,Co,Fe)O phase into the spinel structure ($MnCo_2O_4$), i.e., after heat treatment for 100 h at 850 °C (see Fig. 5d) much lower values for the local Young's modulus were measured than for the cases where a two-phase structure exists, i.e., where the phase transformation is only partly proceeded (here for 10 h at 700 °C and 100 h 700 °C).

Residual Stress Depth Distribution

In Fig. 6, the residual stresses depth distributions that are determined by incremental hole drilling are shown. In order to accurately determine the residual stress depth distribution for MCF coatings, case-specific calibration was applied and as input data the depth distributions of the elastic constants for were used, which were determined by means of instrumented indentation testing (see Fig 5). For the substrate material, the Young's modulus and the Poisson's ratio were set to 200 GPa and 0.3, respectively. For all MCF coatings studied here, the strain relaxations measured in three definite directions (0°, 45°, 90°) while

stepwise drilling the hole are almost similar, which indicates that the residual stress distributions induced by plasma spraying and subsequent heat treatments are almost axisymmetric. In consequence, only the average values are presented and the error bars indicate the standard deviations due to the small differences in direction-dependent strain relaxations. In addition to the residual stresses, Fig. 6 also shows the approximate mismatch in the CTE values between MCF coatings and substrate.

In this regard, Vegard's rule of mixtures was applied to determine the approximate mean CTE of the mixture between salt rock structure and spinel structure according to

$$\Delta\alpha_{MCF} = \alpha_{(Mn,Co)O}(1 - f_{MnCo_{1.9}Fe_{0.1}O_4}) + \alpha_{MnCo_{1.9}Fe_{0.1}O_4}(f_{MnCo_{1.9}Fe_{0.1}O_4}) - \alpha_{substrate}.$$

(Eq 5)

Here, $\alpha_{(Mn,Co)O}$ is the CTE of the (Mn,Co)O phase, $\alpha_{MnCo_{1.9}Fe_{0.1}O_4}$ is the CTE of the $MnCo_{1.9}Fe_{0.1}O_4$ phase, $\alpha_{substrate}$ is the CTE of the substrate and $f_{MnCo_{1.9}Fe_{0.1}O_4}$ is the average volume fraction of the $MnCo_{1.9}Fe_{0.1}O_4$ spinel phase.

In Fig. 6(a), the residual stress depth distribution for the as-sprayed condition is shown. An upper limit for the residual stresses that are expected for the quenching and the thermal stresses can be estimated by Eq 1 and 2, respectively. Prospectively, it is assumed that the temperature of individual splats during spraying was about 1700 °C, which is the approximate value of the melting temperature of $MnCo_{1.9}Fe_{0.1}O_4$, and the temperature of the substrate was about 200 °C. According to Eq 1, the estimated quenching stresses σ_q are about 4 GPa and the additional thermal stresses σ_{th} can be estimated to a value of about 100 MPa using Eq 2.

Hence, the resulting estimated value for the residual stresses in the MCF coating is extremely higher than the residual stresses that were determined by means of the incremental hole drilling method. That means that the high-quenching stress that is expected in the MCF coating in theory must be largely relaxed during layer deposition (Ref 6). This is surely promoted by the inhomogeneous structure of the as-sprayed state, i.e., by the rather high pore density and by the distribution of pores as well as the micro-crack formation during cooling. Since experimentally rather low tensile residual stresses are determined after thermal spraying, it appears that the residual stress development is dominated by the formation of thermal stresses.

In Fig. 6(b), (c) and (d), the residual stress depth distributions after defined thermal aging treatments are presented.

The residual stress distribution after heat treatment for 10 h at 700 °C indicates (Fig. 6b) that again tensile
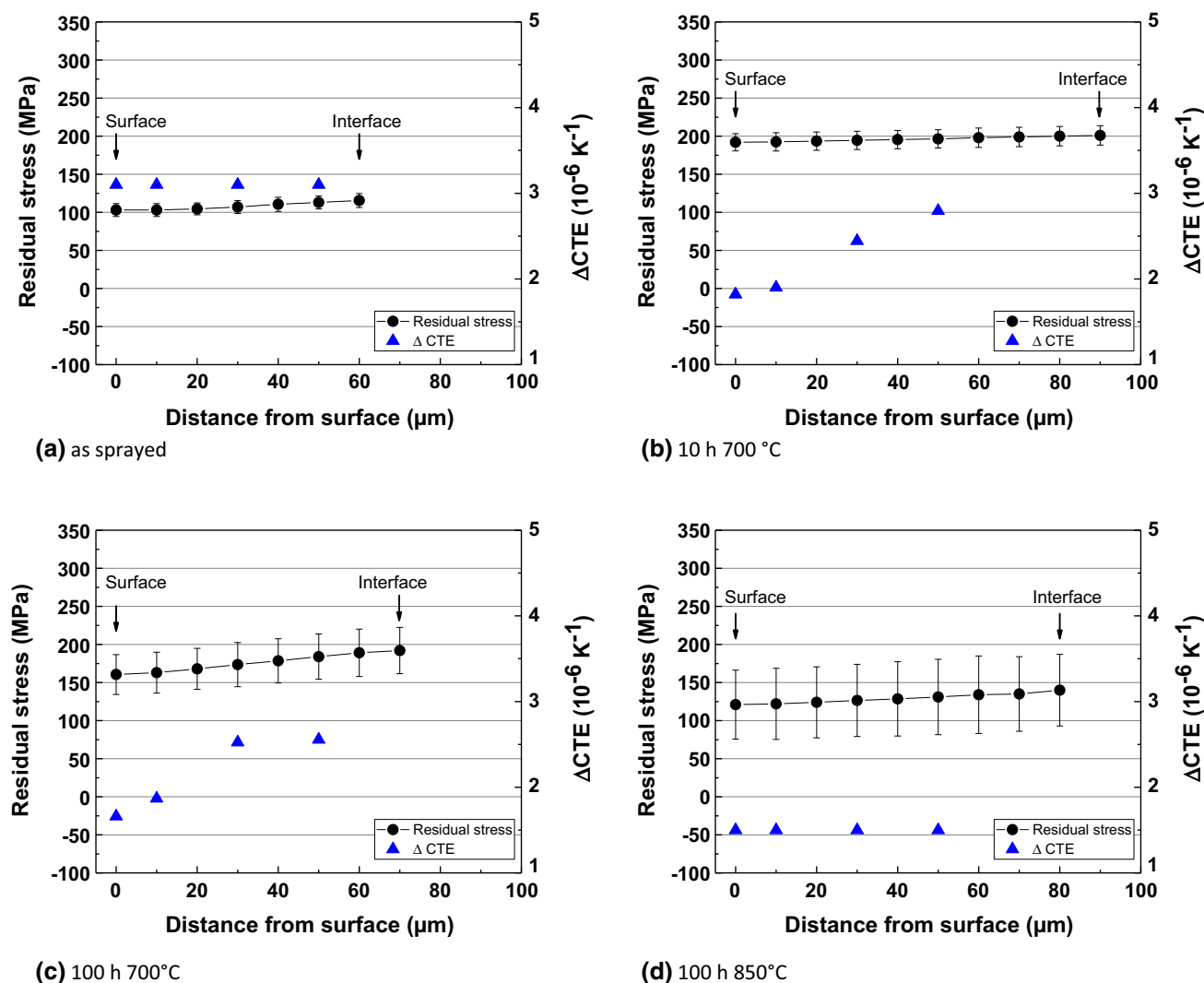
(a) as sprayed

(b) 10 h 700 °C

(c) 100 h 700°C

(d) 100 h 850°C

Fig. 6 Residual stress depth distributions experimentally determined for thermally sprayed MCF coatings subjected to different heat treatment processes (b)-(d) in comparison with the as-sprayed condition (a). In addition, the estimated mismatch in the depth-dependent CTE value is plotted

residual stresses exist, which are almost uniform through the depth with an average value of about 200 MPa. This means that compared to the as-sprayed condition the residual stress depth distribution is shifted upwards to higher tensile residual stresses compared to the as-sprayed condition. Assuming that during this long-lasting annealing at high temperature, the process-induced residual stresses in the coating can relax through plastic deformation in the steel substrate with its low high-temperature strength and the source of the tensile residual stresses for the heat-treated state is the mismatch in the CTE and the temperature difference (Fig. 6b-d). Here, from theoretical consideration, tensile residual stresses up to about 360 MPa might be expected in the coating (according to Eq 2).

With respect to the CTE course, which indicate lower mismatch values at the very surface and higher ones toward

the interface (Fig. 6b and c), which is due to the partial phase transformation over the coating thickness, a slight gradient in tensile residual stresses might be expected. The higher tensile residual stresses that should form right at the interface will be partly accommodated by plastic deformation in the steel substrate during slow cooling down. The slightly lower tensile residual stresses for the state after 100-h heat treatment at 700 °C at the very surface of the coated sample can be explained by the small increase in pore density (see Fig. 5c). Furthermore, the slight gradient observed in Fig. 6(c) can be promoted by the progressing phase transformation from the salt rock phase into the spinel structure, which is accompanied by a volume expansion up to about 21% (Ref 10). The volume expansion should shift the local residual stress distribution at the surface slightly toward the compressive regime.

Thermal aging for 100 h at higher temperatures, i.e., at 850 °C, leads to further reduced tensile residual stresses in the MCF coating with an average value of about 120 MPa (Fig. 6d). Again the course shows a slight gradient in depths with slightly higher tensile residual stresses of about 150 MPa at the interface. However, the gradient is rather small and the small changes are within the resolving capacity of the residual stress analysis method. Apart of this, much lower tensile residual stresses occur as expected from the nominal mismatch in CTE after cooling down from 850 °C. Again, this can be explained by the relaxation of stresses due to plastic deformation of the Crofer 22 APU substrate, which is even more effective at temperatures up to 850 °C. Furthermore, the change of porosity has an effect on the local constraint and hence on the evolution of macroscopic thermal strains in the coating system. This means that lower amount of thermal strain will be transferred with increasing porosity, which leads to a reduction in the effective thermal strain built-up and therefore to lower tensile residual stresses for the present MCF coating system. For the state that was heat-treated for 100 h at 850 °C, a slight increase in porosity was determined, which contribute to this effect.

The stability of SOFC stacks with APS-sprayed MCF protection layers and Crofer 22 APU as interconnect steel was already demonstrated in long-term operation tests in (Ref 22) for 1240 h at 700 °C and in (Ref 23) for 34.000 h at 700 °C. It has been shown that the Cr degradation and its deposition on the cathode under load was effectively reduced by means of the manganese-cobalt-ferrite (MCF) chromium retention coating and that the cell degradation is only moderate showing degradation rates less than 0.3% per 1.000 h for the average voltage (Ref 23).

For the application of SOFCs, the results about the microstructural development of APS-processed MCF coatings after thermal aging underline this long-term performance and suggest the following: Usually, APS processing of ceramic coatings is prone to cause layers being interspersed with cracks and further imperfections. The thermal aging was envisaged to simulate the loading situation during field application of the SOFC stacks. In this regard, the observed consolidation of the material together with the phase transformation causes a high sintering of the material during application features a self-repairing effect and results in dense and gas-tight protection layers. The investigations have shown that the mechanical properties are mainly maintained. Hence, in conclusion the microstructural changes due to thermal aging effectively improve the integrity of the coatings and contribute to the very good long-term stability of the SOFC stacks observed

(Ref 22, 23). Finally, the relatively small tensile residual stresses determined by means of incremental hole drilling will certainly not act as a source for flaking or spalling of the protection layers.

Summary and Conclusion

MCF protective layers deposited on Crofer 22 APU via atmospheric plasma spraying (APS) were characterized in regard to the local microstructure, pore distributions and pore shapes, phase fractions, micro-hardness, Youngs' modulus and residual stresses through the coating thickness. The as-sprayed state was compared with samples that were subjected to various longtime heat treatments, i.e., for 10 and 100 h at 700 °C and for 100 h at 850 °C. The main conclusions of the investigations can be wrapped-up as follows:

- The crystal structure of the as-sprayed state was determined as metastable rock salt structure due to rapid solidification during thermal spraying.
- During the various heat treatments, the rock salt structure gradually transformed to the spinel structure. The phase transformations were initiated at the surface due to the high oxygen partial pressure. The gradual phase transformation is accompanied by a densification of the structure; hence, in general pore density deceases.
- In the as-sprayed state, flat shape pores exist, which partly vanish or change their shape to more globular appearance.
- The gradual phase transformation and the change in porosity has an effect on the mechanical properties as, e.g., on the local materials stiffness (Youngs' modulus), which must also be considered for the residual stress analysis.
- The incremental hole drilling method is well suited to determine the residual stress depths distribution in the MCF coatings. Using this approach, low tensile residual stresses with values slightly above 100 MPa were determined for the as-sprayed condition. This can be attributed to thermal stresses that most likely develop through atmospheric plasma spraying
- After longtime heat treatment, the process-induced residual stress relaxes through plastic deformation of the steel substrate at the interface. The resulting tensile residual stresses after cooling down from heat treatment temperature are dominated by the local mismatch in the CTE values. In all cases, almost homogeneous residual

stress distribution through depths was determined and no residual stress depth gradients were determined in the MCF coatings as expected from the microstructure gradient. This can mainly be attributed to local relaxations of residual stresses through plastic accommodation of stresses by the Crofer steel substrate.

- The long-term thermal aging aimed at simulating the SOFC stack operation. The microstructural development observed in that respect increases the integrity of the coatings aroused by the high sintering that result in dense and gas-tight protection layers. The low tensile residual stresses in the coating remaining after thermal aging will not contribute to early failure due to flaking or spalling.

References

1. Z. Yang, G.G. Xia, X.H. Li, and S. Jeffry (Mn,Co)3O4 Spinel Coatings on Ferritic Stainless Steels for SOFC Interconnect Applications, *Int. J. Hydrogen Energy*, 2007, **32**, p 3648-3654
2. S.P.S. Badwal, R. Deller, K. Foger, Y. Ramprakash, and J.P. Zhang, Interaction Between Chromia Forming Alloy Interconnects and Air Electrode of Solid Oxide Fuel Cells, *Solid State Ion.*, 1997, **99**, p 297-310
3. H. Wenhua, G. Srikanth, B.P. Uday, and N.B. Soumendra, Evaluation of Electrophoretically Deposited CuMn1.8O4 Spinel Coatings on Crofer 22 APU for Solid Oxide Fuel Cell Interconnects, *J. Electrochem. Soc.*, 2008, **155**(11), p 1161-1167
4. R. Vaßen, N. Grünwald, D. Marcanoa, N.H. Menzler, R. Mücke, D. Sebold, Y.J. Sohn, and O. Guillon, Aging of Atmospherically Plasma Sprayed Chromium Evaporation Barriers, *Surf. Coat. Technol.*, 2016, **291**, p 115-122
5. L. Blum, P. Batfalsky, Q. Fang, L.G.J. de Haart, J. Malzbender, N. Margaritis, N.H. Menzler, and R. Perters, SOFC Stack and System Development at Forschungszentrum Jülich, *J. Electrochem. Soc.*, 2015, **162**(10), p 1199-1205
6. S. Kuroda and T.W. Clyne, The Quenching Stress in Thermally Sprayed Coatings, *Thin Solid Films*, 1991, **200**, p 29-66
7. H.C. Back, M. Mutter, J. Gibmeier, R. Mücke, and R. Vaßen, Residual Stress Depth Distributions for Atmospheric Plasma Sprayed MnCo1.9Fe0.1O4 Spinel Layers on Crofer Steel Substrate, *Mater. Sci. Forum*, 2017, **905**, p 174-181
8. Material Data Sheet No. 4046: VDM® Crofer 22 APU (2010) VDM Metals GmbH, Werdohl, Germany
9. M. Mellali, A. Grimaud, A.C. Leger, P. Fauchais, and J. Lu, Alumina Grit Blasting Parameters for Surface Preparation in the Plasma Spraying Operation, *J. Therm. Spray Technol.*, 1997, **6**(2), p 217-227
10. N. Grünwald, D. Sebold, Y.J. Sohn, N.H. Menzler, and R. Vaßen, Self-Healing Atmospheric Plasma Sprayed Mn1.0Co1.9Fe0.1O4 Protective Interconnector Coatings for Solid Oxide Fuel Cells, *J. Power Sources*, 2017, **363**, p 185-192
11. C.T. Rueden, J. Schindelin, M.C. Hiner et al., ImageJ2: ImageJ for the Next Generation of Scientific Image Data, *BMC Bioinform.*, 2017, **18**, p 529. https://doi.org/10.1186/s12859-017-1934-z
12. L. Lutterotti, D. Chateigner, S. Ferrari, and J. Ricote, Texture, Residual Stress and Structural Analysis of Thin Films Using a Combined X-Ray Analysis, *Thin Solid Films*, 2004, **450**, p 34-41
13. H. Bordeneuve, C. Tenailleau, S. Guillemet-Fritsch, R. Smith, E. Suard, and A. Rousset, Structural Variations and Cation Distributions in $Mn_{3-x}Co_xO_4$ $(0 \leq x \leq 3)$ Dense Ceramics Using Neutron diffraction Data, *Solid State Sci.*, 2010, **12**, p 379-386
14. ASTM International, *E837-13a Standard Test Method for Determining Residual Stresses by the Hole-Drilling Strain-Gage Method*, ASTM International, West Conshohocken, PA, 2013, https://doi.org/10.1520/E0837-13A
15. G.S. Schajer, Measurement of Non-uniform Residual Stresses Using the Hole-Drilling Method. Part I—Stress Calculation Procedures, *J. Eng. Mater. Technol.*, 1988, **110**(4), p 338-343
16. E. Obelode and J. Gibmeier, Residual Stress Analysis on Thick Film Systems by the Incremental Hole-Drilling Method—Simulation and Experimental Results, *Exp. Mech.*, 2013, **53**, p 965-976
17. N. Grünwald, *Selbstheilende Plasmagespritzte Mn₁,₀Co₁,₉Fe₀,₁O₄ SCHUTZSCHICHTEN in Festoxidbrennstoffzellen*, Doctoral Thesis, Ruhr-Universität Bochum, Universität, Bochum, 2018
18. N. Uchida and S. Shoichi, Elastic Constants and Acoustic Absorption Coefficients in MnO, CoO, and NiO Single Crystals at Room Temperature, *J. Acoust. Soc. Am.*, 1972, **51**, p 1602-1605
19. I. Suzuki, S.I. Okajima, and K. Seya, Thermal Expansion of Single Manganasite, *J. Phys. Earth*, 1979, **27**, p 63-69
20. P. Kofstad, *High Temperature Corrosion*, Elsevier Applied Science, Amsterdam, 1988
21. Metallic Materials—Instrumented Indentation Test for Hardness and Materials Parameters—Part 1: Test Method (ISO 14577-1:2015), Beuth-Verlag Berlin
22. A. Beez, X. Yin, N.H. Menzler, R. Spatschek, and M. Bram, Insight into the Reaction Mechanism of (La0.58Sr0.40)(Co0.20-Fe0.80)O3-δ Cathode with Volatile Chromium Species at High Current Density in a Solid Oxide Fuel Cell Stack, *J. Electrochem. Soc.*, 2017, **164**, p F3028-F3034
23. S.M. Groß-Barsnick, Q. Fang, P. Batfalsky, L. Niewolak, L. Blum, and W.J. Quadakkers, Post-test Characterization of Metallic Materials and Adjacent Components in an SOFC Stack After 34,000 h Operation at 700 °C, *Fuel Cells*, 2019, **19**, p 84-95

Publisher's Note Springer Nature remains neutral with regard to jurisdictional claims in published maps and institutional affiliations.